Atmos. Chem. Phys. Discuss., 13, 22249–22296, 2013
www.atmos-chem-phys-discuss.net/13/22249/2013/
doi:10.5194/acpd-13-22249-2013

Atmospheric Chemistry and Physics
Discussions
Open Access

Cloud-scale ice supersaturated regions spatially correlate with high water vapor heterogeneities

M. Diao[1,2], M. A. Zondlo[1,2], A. J. Heymsfield[3], L. M. Avallone[4], M. E. Paige[5], S. P. Beaton[6], T. Campos[7], and D. C. Rogers[6]

[1]Dept. of Civil and Environmental Engineering, Princeton University, New Jersey, 08544, USA
[2]Ctr. for Mid-Infrared Technologies for Health and the Environment, Princeton University, New Jersey, 08544, USA
[3]Mesoscale and Microscale Meteorology, National Center for Atmospheric Research, Boulder, Colorado, 80301, USA
[4]Department of Atmospheric and Oceanic Sciences, University of Colorado, USA
[5]Southwest Sciences, Inc., Santa Fe, New Mexico, 87505, USA
[6]Earth Observing Laboratory, National Center for Atmospheric Research, Broomfield, Colorado, 80021, USA
[7]Atmospheric Chemistry Division, National Center for Atmospheric Research, Boulder, Colorado, 80301, USA

Received: 29 July 2013 – Accepted: 22 August 2013 – Published: 27 August 2013

Correspondence to: M. A. Zondlo (mzondlo@princeton.edu)

Published by Copernicus Publications on behalf of the European Geosciences Union.

ACPD
13, 22249–22296, 2013

Cloud-scale ice supersaturated regions

M. Diao et al.

Abstract

Cirrus clouds have large yet uncertain impacts on the Earth's climate. Ice supersaturation (ISS) – where the relative humidity with respect to ice (RHi) is greater than 100 % – is the prerequisite condition of ice nucleation. Here we use 1 Hz (∼ 230 m) in situ aircraft-based observations from 87° N–67° S to analyze the spatial characteristics of ice supersaturated regions (ISSRs). The median length of 1-D horizontal ISSR segments is found to be very small (∼ 1 km), which is two orders of magnitude smaller than previously reported. To understand the conditions of these small scale ISSRs, we compare individual ISSRs with their horizontally adjacent subsaturated surroundings and show that 99 % and 73 % of the ISSRs are moister and colder, respectively. When quantifying the contributions of water vapor (H_2O) and temperature (T) individually, the magnitudes of the differences between the maximum RHi values inside ISSRs (RHi_{max}) and the RHi in subsaturated surroundings are largely derived from the H_2O spatial variabilities (by 88 %) than from those of T (by 9 %). These features hold for both ISSRs with and without ice crystals present. Similar analyses for all RHi horizontal variabilities (including ISS and non-ISS) show strong contributions from H_2O variabilities at various T, H_2O, pressure (P) and various horizontal scales (∼ 1–100 km). Our results provide a new observational constraint on ISSRs on the microscale (∼ 100 m) and point to the importance of understanding how these fine scale features originate and impact cirrus cloud formation and the RHi field in the upper troposphere (UT).

1 Introduction

Cirrus clouds, located in the UT and composed of ice crystals, cover ∼ 30 % of the Earth's surface (Wylie and Menzel, 1999). As a major uncertainty in climate modeling (Solomon et al., 2007), the magnitude and sign (cooling or warming) of cirrus clouds' radiative forcing are not only influenced by macroscopic properties, such as coverage, thickness and height, but also by microphysical properties, such as ice crystal number

ACPD
13, 22249–22296, 2013

density and size distribution (Liou, 1992). In order to understand the microphysical properties of cirrus clouds, it is crucial to analyze the initial conditions of cirrus cloud formation, i.e., the conditions of ISS. For example, the frequency distribution of ISS can help us to estimate the influences of different freezing mechanisms for cirrus cloud formation (Cziczo et al., 2013), while the transition from clear-sky ISS to the ISS with ice crystals can help us to understand the formation and evolution of ice crystal regions (Diao et al., 2013).

Ice nucleation happens once RHi reaches the nucleation threshold (RHi_{nucl}) (Koop et al., 2000; Murphy and Koop, 2005; Peter et al., 2006). By definition, RHi = $e/e_s \times 100\,\%$, where e is the H_2O partial pressure and e_s is the saturation vapor pressure from the Clausius-Clapeyron Equation. It is crucial to understand the temporal and spatial variabilities of RHi, since they determine the time and the location of the ice crystal formation, respectively. However, one of the major difficulties in understanding RHi variability is that the processes influencing it range over numerous orders of magnitude in scale, from the synoptic scale (~ 1000 km) (e.g., Rossby waves), mesoscale (~ 100 km) (deep convection), microscale (~ 100 m, small gravity waves and turbulence) to the micrometer scale (the activation of aerosols) (Heintzenberg and Charlson, 2009; Lynch et al., 2002).

Recently, Wood and Field (2011) showed that the median chord length of cirrus clouds is ~ 1 km based on a combination of in situ aircraft observations, satellite observations and numerical model simulations. However, it is unclear how this small-scale horizontal structure of cirrus clouds forms and what factors contribute to this feature. In particular, although ISS has been widely observed in the atmosphere over various geographical locations (Gettelman et al., 2006; Heymsfield et al., 1998; Kahn et al., 2009; Krämer et al., 2009; Lamquin et al., 2012; Vömel et al., 2002), it has not been analyzed whether the ice supersaturated regions (ISSRs, the regions with spatially continuous ISS) have the microscale structure similar to that of cirrus clouds, nor have the contributing factors been determined.

ACPD
13, 22249–22296, 2013

The spatial characteristics of ISSRs have only been analyzed on the mesoscale based on 1 min averaged (~15 km resolution) aircraft observations (Gierens and Spichtinger, 2000). This study showed that the mean and median lengths of ISSR horizontal 1-D segments are ~150 km and ~50 km, respectively, and also predicted the existence of smaller ISSRs that were not sampled. Other in situ observations at higher resolution (1 Hz), such as Krämer et al. (2009) and Ovarlez et al. (2002), analyzed the RHi distribution for the integration of all the 1 Hz data, but did not address how individual ISSRs are distributed in the spatial view or what factors contribute to their spatial characteristics.

To help understand the spatial characteristics of ISSRs, it is important to understand the spatial variabilities of T and H_2O, as they directly influence the spatial variabilities of RHi. Spichtinger et al. (2003) used Microwave Limb Sounder observations on the ~200 km scale and showed that ISSRs, on average, have colder T and higher moisture than subsaturated air. However, it has not been analyzed how the T and H_2O spatial variabilities quantitatively contribute to the higher RHi values inside individual ISSRs. In addition, when deriving the general RHi spatial variability on the microscale, it is unknown whether H_2O and T spatial variabilities have similar contributions or if one is more dominant than the other.

To compare the contributions of H_2O and T to RHi variabilities, the Clausius-Clapeyron equation is usually used to decompose the changes of RHi into the changes of H_2O and T. For example, Spichtinger et al. (2005a) and Spichtinger et al. (2005b) used radiosonde data on the ~100 km scale to analyze the formation of ISSRs in the Lagrangian view by large scale dynamics, such as gravity waves and warm conveyor belts. They pointed out the importance of large-scale cooling during the time evolution of ISSRs based on 100 km-scale Lagrangian model simulations. However, the conditions of ISSRs below the 100 km scale have not been analyzed, and it is unclear if T spatial variability is the dominant contribution to RHi spatial variability in the Eulerian view.

ACPD
13, 22249–22296, 2013

In this study, we analyze the individual conditions of ISSRs based on 1 Hz resolution aircraft observations. This study provides a large number of case studies of ISSRs on the microscale based on the Eulerian view in situ observations. Direct comparisons between ISSRs and their adjacent subsaturated surrounding environments are conducted in order to help understand the factors contributing to the spatial characteristics of ISSRs.

2 Data sets and instrumentation

In this work, the spatial variabilities of ISS and RHi are analyzed based on the 1 Hz (∼ 230 m) in situ observations made from the National Science Foundation (NSF) Gulfstream-V research aircraft. Two flight campaigns are combined for a comprehensive dataset over various latitudes, altitudes and seasons. The NSF Stratosphere Troposphere Analyses of Regional Transport 2008 (START08) campaign (Pan et al., 2010) sampled the UT/LS over North America in April–June 2008, providing ∼ 90 transects across the thermal tropopause. The NSF HIAPER Pole-to-Pole Observations (HIPPO) Global field campaign (Wofsy et al., 2011) provided an extensive latitudinal coverage (87° N–67° S) over the central Pacific Ocean from 2009 to 2011, with ∼ 600 vertical transects from the surface to the tropical UT or the extratropical UT/LS. The flight tracks of the START08 and HIPPO campaigns being analyzed in this study are shown in Fig. 1. Flights without H_2O observations are not shown here.

Water vapor was measured by the 25 Hz, open-path Vertical Cavity Surface Emitting Laser (VCSEL) hygrometer (Zondlo et al., 2010). The accuracy and precision of H_2O measurements are 6 % and ≤ 1 %, respectively. The H_2O measurements were averaged to 1 s for consistency with the *T* measurements. The open-path design of the VCSEL hygrometer is critical for the fast response of H_2O measurements, as surface absorption and sampling problems may complicate the response time of closed-path systems. The fast response of H_2O measurements here provides the fundamental technical support to our analyses of the contributions of H_2O and T fluctuations to the RHi spatial variabilities.

Temperature measurements were recorded by the Rosemount temperature probe. The accuracy and precision of T measurements are 0.5 K and 0.01 K, respectively. The uncertainties in RHi were 8–10 % at 233–205 K after combining the uncertainties from the VCSEL hygrometer (6 %) and the T probe (±0.5 K). We do not apply higher frequency observations to our analyses because no fast T measurements (< 1 Hz) were available in HIPPO, and the fast (sub-Hz) T measurements in START08 were complicated by the presence of ice crystal particles. For these reasons, we only use 1 Hz data in our analyses.

To compare the ISS variability between regions with and without ice crystals, we use ice crystal concentration measurements to separate these two types of regions. In START08, the ice crystal concentrations were measured by the HIAPER Small Ice Detector Probe (SID-2H) instrument (Cotton et al., 2010). The measurement range of SID-2H is 1–50 µm. During the HIPPO Global campaign deployments #2–5, ice crystal concentrations were measured by the 2DC ice probe (Korolev et al., 2011). The 2DC ice probe has a measurement range of 25–800 µm, which reports ice crystal number density Nc (in L^{-1}). Since the ice crystal concentrations were not measured in HIPPO deployment #1, we only compare the ISSRs with and without the presence of ice crystals during START08 and HIPPO deployments #2–5. Here we use the terminology of "in-cloud" to represent the regions with the presence of ice crystals. For SID-2H measurements, we define the "in-cloud" regions as locations where the total ice particle concentrations are greater than 0.06 cm^{-3} during the 1 Hz measurements. For 2DC measurements, we define the "in-cloud" regions to be where Nc is greater than zero. The remaining regions are considered to be "clear-sky" regions. We used 0.06 cm^{-3} as the threshold for SID-2H instrument because it represents greater than one particle per second under the sampling rate of 16 $cm^3\,s^{-1}$. This measurement range is where the SID-2H ice probe functions well for distinguishing between ice crystals and liquid

ACPD
13, 22249–22296, 2013

Cloud-scale ice supersaturated regions

M. Diao et al.

aerosols. We note that these terms of "in-cloud" and "clear-sky" only represent the conditions of 1-D flight segments.

Other measurements that have been used to help interpret the results include ozone (O_3), carbon monoxide (CO), ice water content and vertical wind velocity (w). O_3 was measured by the NCAR dual-beam ultraviolet absorption photometer with an accuracy of 9 % and precision of 0.8 ppbv (Tilmes et al., 2010). CO was measured using a vacuum ultraviolet resonance fluorescence with an accuracy of 5 % and precision of 5 % (Tilmes et al., 2010). Ice water content was measured by the University of Colorado (CU) tunable diode laser hygrometer with an accuracy of 20–25 % and precision of 5 % (Davis et al., 2007). The vertical velocity speed (w) was measured by the Radome wind gust package on the GV aircraft. The accuracy and precision of w measurements are $0.1\,\mathrm{m\,s^{-1}}$ and $0.012\,\mathrm{m\,s^{-1}}$, respectively.

Because any synchronization delays between the H_2O and T measurements would impact our analyses of their contributions to the RHi fluctuations, we demonstrate the in-flight synchronization between the T and H_2O measurements with the special case of a gravity wave observed in START08 Research Flight (RF) 08 (Fig. 2). We note that this gravity wave has unusually high frequency and magnitude as well as a clearly observable wave structure, which were not typically seen during the START08 and HIPPO flight campaigns. In general, as the aircraft horizontally transects through a gravity wave near the tropopause, the H_2O concentration and T values are expected to anticorrelate with each other. In this case, the gravity wave has ~ 10 oscillations with an average period of ~ 8 s (~ 1800 m). The peaks of H_2O concentration match well with the troughs of T values in individual periods, which demonstrate that T and H_2O measurements have fast, synchronized response to the fluctuations of the atmospheric conditions at 1 Hz resolution.

ACPD
13, 22249–22296, 2013

3 Methods

3.1 Method for analyzing RHi spatial variability

Based on the Clausius-Clapeyron equation, the variability of RHi is directly contributed by the variabilities of H_2O and T. Although previous studies have analyzed the spatial variabilities of T and H_2O (Cho et al., 2000) and the variance scaling of T and H_2O (Kahn and Teixeira, 2009; Kahn et al., 2011), it is still unclear for individual ISSRs how the higher RHi values inside ISSRs than their adjacent subsaturated air are derived from T and H_2O spatial variabilities. In addition, although it has been shown for the boundary layer that T contribution to RH variability becomes more important from mesoscale to microscale (Price and Wood, 2002), it has not been analyzed for the RHi in the UT whether the T contribution follows similar trend.

To quantify the contributions from H_2O and T spatial variabilities to the RHi spatial variability, we separate the change of RHi (dRHi) into two parts: the contributions from H_2O partial pressure variability ($d\mathrm{RHi}_q$) and those from T variability ($d\mathrm{RHi}_T$). Applying the Taylor expansion to dRHi, we get:

$$d\mathrm{RHi} = d\frac{e}{e_\mathrm{s}} = ed\frac{1}{e_\mathrm{s}} + \frac{1}{e_\mathrm{s}}de = d\mathrm{RHi}_T + d\mathrm{RHi}_q; \tag{1a}$$

Here e is the H_2O partial pressure, and e_s is the saturation vapor pressure over ice calculated based on the equation from Murphy and Koop (2005). Because aircraft sampling is discretely distributed, we use the difference between two points as an approximation of the derivative. We assume that the magnitudes of $d(1/e_\mathrm{s})$ and de terms are relatively small, so that only the first terms of the Taylor expansion are considered in Eqs. (1) and (2):

$$d\frac{1}{e_\mathrm{s}} \approx \Delta\left(\frac{1}{e_\mathrm{s}}\right) = \frac{1}{e_{\mathrm{s},1}} - \frac{1}{e_{\mathrm{s},2}}; \tag{1b}$$

$$de \approx \Delta(e) = e_1 - e_2; \tag{1c}$$

ACPD
13, 22249–22296, 2013

We also separate the changes in e term (de) into the contributions from the variability of H_2O volume mixing ratio (H_2OMR, ppmv) and the variability of total pressure (P, Pa). Similarly, only the first terms of the Taylor expansion are considered for dH_2OMR and dP, assuming that changes are relatively small. The contributions of the H_2OMR and P variabilities to de are defined as de_{H_2OMR} and de_P, respectively:

$$de = d(H_2OMR \cdot P) = P \cdot dH_2OMR + H_2OMR \cdot dP = de_{H_2OMR} + de_P \tag{2a}$$

$$dH_2OMR \approx \Delta(H_2OMR) = H_2OMR_1 - H_2OMR_2; \tag{2b}$$

$$dP \approx \Delta(P) = P_1 - P_2; \tag{2c}$$

To directly compare how H_2O and T variabilities contribute to individual ISSR conditions, we compare the RHi values inside and outside of each ISSR. We calculated the difference between the RHi_{max} inside an ISSR ($RHimax_{inside}$) and the RHi of the horizontal adjacent subsaturated regions ($RHi_{outside}$). This difference is defined as $dRHi_{max}$. Here we use the mean RHi of the horizontally adjacent (±1 s) subsaturated air as representative of $RHi_{outside}$, although other larger scales (e.g., ±2 s, ±3 s, up to ±30 s) of subsaturated conditions have also been tested to verify our results. We apply Eqs. (1) and (2) to $dRHi_{max}$ to quantify how $dRHi_{max}$ in each ISSR segment is composed of a pair of $dRHi_q$ and $dRHi_T$.

Similarly, we analyze the horizontal spatial variabilities of all RHi (including both ISS and non-ISS) using Eqs. (1) and (2). Here the RHi difference between the mean RHi values of two horizontally (dP<1 hPa) adjacent segments is defined as $dRHi$. Different scales of horizontal segments are analyzed from ~230 m up to ~115 km. The maximum scale of the horizontal segment is limited to 115 km (~500 s) because of the strict horizontal restriction (dP<1 hPa) and the decreasing number of consecutive

ACPD
13, 22249–22296, 2013
Cloud-scale ice supersaturated regions
M. Diao et al.

flight samples with the increasing scale. We apply Eqs. (1) and (2) to the dRHi of each pair of horizontal adjacent segments and quantify how the fluctuations of H_2O and T contribute to each dRHi.

3.2 Method for analyzing the mean absolute deviation of RHi

Another similar method to analyze contributions to the RHi field is to examine the variabilities around the mean value for a certain length scale. In this regard, we also analyze the RHi horizontal spatial variability in terms of the mean absolute deviation of RHi (σRHi). σRHi is calculated for individual horizontal (dP<1 hPa) segments during the aircraft sampling by comparing each 1 Hz RHi value within that segment with the mean RHi value (Eq. 3a). The contributions from the variabilities of H_2O and T to the magnitude of σRHi are defined as σRHi_q and σRHi_T in Eqs. (3b) and (3c), respectively. According to these definitions, the higher H_2O concentrations (lower T values) relative to the mean H_2O (T) values will provide positive contributions to the σRHi value. On the other hand, the lower H_2O concentrations (higher T values) relative to the mean H_2O (T) values will provide negative contributions to the σRHi value. Thus, the calculations of σRHi_q and σRHi_T consider the signs (positive or negative) of the H_2O and T contributions.

$$\sigma\text{RHi} = \frac{\sum_{k=1}^{N}(|\text{RHi}_k - \overline{\text{RHi}}|)}{N-1}, \tag{3a}$$

$$\sigma\text{RHi}_q = \frac{\sum_{k=1}^{N}(\text{sgn}(x_q)|\overline{\tfrac{1}{e_s}}(e_k - \overline{e})|)}{N-1}, \tag{3b}$$

ACPD
13, 22249–22296, 2013
Cloud-scale ice supersaturated regions
M. Diao et al.

$$\sigma\mathrm{RHi}_T = \frac{\sum_{k=1}^{N}(\mathrm{sgn}(x_T)|\overline{e}(\frac{1}{e_{s_k}} - \overline{\frac{1}{e_s}})|)}{N-1}, \tag{3c}$$

$$\mathrm{sgn}(x_q) = 1, \mathit{if}(\mathrm{RHi}_k - \overline{\mathrm{RHi}})(\overline{\frac{1}{e_s}}(e_k - \overline{e})) \geq 0,$$

$$\mathrm{sgn}(x_q) = -1, \mathit{if}(\mathrm{RHi}_k - \overline{\mathrm{RHi}})(\overline{\frac{1}{e_s}}(e_k - \overline{e})) < 0,$$

$$\mathrm{sgn}(x_T) = 1, \mathit{if}(\mathrm{RHi}_k - \overline{\mathrm{RHi}})(\overline{e}(\frac{1}{e_{s_k}} - \overline{\frac{1}{e_s}})) \geq 0,$$

$$\mathrm{sgn}(x_T) = -1, \mathit{if}(\mathrm{RHi}_k - \overline{\mathrm{RHi}})(\overline{e}(\frac{1}{e_{s_k}} - \overline{\frac{1}{e_s}})) < 0,$$

where N is the sample size; $\overline{\mathrm{RHi}}$, $\overline{\frac{1}{e_s}}$ and $\overline{e}$ are the mean values of RHi, $\frac{1}{e_s}$ and e in the sampling range, respectively. Similar to the dRHi analyses of the horizontal RHi variability, the maximum scale of σRHi is also limited to 115 km ($N = 500$) because of the strict horizontal restriction (dP<1 hPa) and the decreasing number of consecutive flight samples with increasing scale. We note that the current method differs from the previous variability analyses of Gierens et al. (2007), which decomposed the standard deviation of RHi into the standard deviations of H_2O and T. Because the standard deviations do not consider the signs of the fluctuations, the previous analyses did not account for the signs of the contributions of T and H_2O variabilities to RHi variability.

ACPD
13, 22249–22296, 2013

4 Results and discussion

4.1 Overall aircraft sampling of ISS and ISSRs

The whole dataset consists of ∼ 217 h of 1 Hz observations at $T \leq -40\,^{\circ}$C (∼ 62 h from START08, ∼ 155 h from HIPPO). Unless notified otherwise, we restrict our analyses to $T \leq -40\,^{\circ}$C to ensure that no ambiguities from supercooled liquid water are involved (Murphy and Koop, 2005). The overall distribution of the observations at $T \leq -40\,^{\circ}$C is illustrated in Fig. 3 in the latitudinal and vertical view. Here the number of observations is binned by 10° in latitudes and 25 mb in pressure. Figure 3 shows that our observations from the HIPPO and START08 campaigns cover a wide latitudinal range (87° N–67° S) and vertical range (150–550 mb).

Of the 217 h at $T \leq -40\,^{\circ}$C, there are ∼ 11 h of ISS observations (5 %), which are composed of 1542 individual ISSR segments. Here an ISSR is defined as the 1-D segment where ISS is observed to be spatially continuous. Similar to previous analyses, ISSRs include both clear-sky and in-cloud conditions (Spichtinger et al., 2005b). For the dataset with ice particle measurements (i.e., START08 campaign and HIPPO deployments #2–5), 97 % of total observations at $T \leq -40\,^{\circ}$C were in clear sky and 3 % were in cloud. For the clear-sky conditions, 5 % were ice-supersaturated. For the in-cloud conditions, 54 % were ice-supersaturated.

To demonstrate the general consistency with past work for in-cloud measurements, we examine the probability density function (PDF) of the RHi for in-cloud conditions. The PDF of 1 Hz in-cloud RHi in START08 and HIPPO#2–5 campaigns peaks around 95.5–98.5 % (Fig. 4). Ovarlez et al. (2002) analyzed 1 Hz aircraft observations at Prestwick, Scotland (55° N) and showed that the PDF of in-cloud RHi peaks at 97.5 % at $T \leq -40\,^{\circ}$C, which is very consistent with our observations. For the larger scale (∼ 45 km) RHi distribution, Kahn et al. (2009) used satellite observations to show that the in-cloud RHi peaks around 80–90 % in the UT. The lower value of the in-cloud RHi peak for the larger scale observations compared with the smaller scale observations is a common feature as discussed by Dickson et al. (2010), since a shallow layer of ice saturation or ISS embedded within a subsaturated layer may be averaged out by satellite retrievals due to their coarse vertical resolutions.

To compare with the previous 1 Hz observations of ISS by Krämer et al. (2009), we analyze the distribution of 1 Hz RHi data at various T (196–233.15 K) for both clear-sky and in-cloud conditions. Figure 5 shows that for both conditions, the RHi observations are almost always at or below the liquid water saturation line calculated based on Murphy and Koop (2005). In addition, the observed ISS is mostly at or below the homogeneous freezing threshold of a liquid droplet with 0.5 µm radius (Koop et al., 2000). These findings are consistent with the RHi distribution with respect to T shown in Krämer et al. (2009) at the same temperature range. We note that the low RHi values around 0–20 % for in-cloud data may represent ice crystals that fall into much drier conditions than their initial formation conditions. We also color coded the RHi data by H_2O mixing ratio and showed that the H_2O mixing ratios of most ISS observations (99 %) are above 20 ppmv (orange to purple color), where complications from calibration artifacts are less problematic.

4.2 Spatial characteristics of ISSRs

We analyze the spatial characteristics of ISSRs in terms of their segment length, spacing and RHi_{max}. Here these spatial characteristics are analyzed in a horizontal Eulerian view, since the aircraft's horizontal true air speed is always at least ~ 25 times greater than its vertical velocity. A representative example of a time series of the aircraft sampling through ISSRs is given in Fig. 6a, which defines the 1-D segment length, spacing and RHi_{max} of the ISSRs. The distributions of these characteristics of all 1542 ISSRs are shown in Fig. 6b. The mean and median of ISSR segment lengths are 3.5 km and 0.7 km, respectively, which are two orders of magnitudes smaller than the previously reported mean (150 km) and median (50 km) ISSR lengths at ~ 15 km resolution (Gierens and Spichtinger, 2000). Besides the small scale of ISSR segment lengths, the 1-D spacings between the ISSR segments are also found to be very small, with the mean and median values of ~ 47 km and ~ 1 km, respectively. The small median value of the spacings suggests that the ISSR segments are closely distributed next to each other, which indicates a very patchy, heterogeneous structure of ISSRs on the microscale that has not been reported before. The 1-D chord lengths of ISSRs cannot be directly treated as the scales of ISSRs in the higher dimensional view, because it is more likely that a larger ISSR will be transected than a smaller one (Gierens and Spichtinger, 2000). Overall, the observed 1-D segment scale of ISSRs (~ 1 km) is comparable to the recently observed 1-D median segment scale of cirrus clouds (~ 1 km) (Wood and Field, 2011), which may indicate a link between the ISS spatial variability and cirrus spatial heterogeneities.

To examine the whether the larger sized ISSRs correlate with larger or smaller RHi values, Fig. 6b shows the RHi_{max} values inside each ISSRs versus the ISSR lengths. The result shows that RHi_{max} increases with increasing ISSR length scale. Although not shown here, the mean RHi values inside ISSRs also increase as the scales of ISSR segment lengths increase. These findings indicate that large scale observations may have biases in estimating RHi_{max} if the small scale ISSR segments have been averaged out due to coarse sampling resolution. The correlation between RHi_{max} and the ISSR scale shows the importance of understanding the scales of the processes that contribute to the formation of ISSRs, since the processes at different scales might not only generate different sizes of ISSRs, but also different values of RHi_{max} and therefore result in different probabilities of ice crystal formation.

4.3 Contributions of H_2O and T spatial heterogeneities to microscale ISSRs

To help quantify the observed horizontal patchiness of ISSRs, we analyze how the higher RHi inside each ISSR segment occurs comparing to the horizontally adjacent subsaturated regions (non-ISSRs). The RHi differences between ISSRs and non-ISSRs fundamentally result from the differences in T and H_2O in these regions. There are three ways that a region becomes an ISSR: (1) colder and moister (in terms of absolute H_2O concentration), (2) colder and drier, or (3) warmer and moister than adjacent non-ISSRs. We categorize the horizontal ISSRs into these three types, which

ACPD
13, 22249–22296, 2013

include 1094 ISSRs on quasi-isobaric levels (dP<1 hPa). In total, 99 % of 1094 horizontal ISSRs have higher H_2O inside than outside (cases 1 + 3), and 73 % have lower T inside than outside (cases 1 + 2) (Fig. 7a). Thus, the ISSRs with higher H_2O concentrations are more frequent than those with lower T.

The frequency analyses above of being colder or moister do not yet address the contributions of H_2O and T in determining the magnitude of the higher RHi inside each ISSR. Therefore, these contributions need to be placed in comparable terms from Eq. (1). The $d\mathrm{RHi}_{\mathrm{max}}$ in each ISSR segment is contributed by a pair of $d\mathrm{RHi}_q$ (Fig. 7b, blue dot) and $d\mathrm{RHi}_T$ (red dot). The slopes of the linear fits represent the ratio of the total contributions, which are 0.88 ± 0.006 and 0.09 ± 0.005 for H_2O and T, respectively (± one sigma represents one standard deviation for all linear fits in this work). Thus the higher $\mathrm{RHi}_{\mathrm{max}}$ magnitude inside ISSRs compared to outside is mainly (88 %) contributed by H_2O variability. The sum of slopes does not exactly equal one since we only consider the first terms of the Taylor expansion of the derivatives of e and $1/e_s$ (see Sect. 3.1). The $d\mathrm{RHi}_q$ term is further analyzed by quantifying the contributions from total pressure and H_2O volume mixing ratio using Eq. (2) (Fig. 7c). The changes in H_2O partial pressure (de) are almost exclusively (100 % ± 0.01 %) the result of the changes of H_2O mixing ratio and not due to total pressure changes.

The above analyses compared ISSRs with their horizontally adjacent (dP<1 hPa) subsaturated air (non-ISSRs) within ±∼ 230 m from the ISSR boundary. In order to demonstrate that the strong contribution of H_2O heterogeneities to $d\mathrm{RHi}_{\mathrm{max}}$ does not vary with the lengths of the non-ISSRs being chosen for the comparisons, we tested our result with various lengths of horizontal adjacent non-ISSRs, ranging from ∼ 230 m to 6.7 km. Beyond ∼ 6.7 km length, the intersection with adjacent ISSR segments limits the data availability. The contribution of H_2O heterogeneities does not vary significantly with the scales of non-ISSRs being chosen for the comparison (Fig. 8).

Considering that the formation of ice crystals inside air parcels can change the distribution of H_2O by depleting the vapor phase, we also analyze how the presence of ice crystals would change the correlations between high H_2O heterogeneities and ISS

Discussion Paper | Discussion Paper | Discussion Paper | Discussion Paper |
ACPD
13, 22249–22296, 2013
Cloud-scale ice supersaturated regions
M. Diao et al.

in the Eulerian view. Using data from the START08 and HIPPO#2–5 campaigns when ice crystals were measured, the ISSRs are separated into regions with and without the presence of ice crystals. The contributions of H_2O and T variabilities to $d\mathrm{RHi}_{max}$ in these two types of ISSRs are analyzed. For these analyses, $d\mathrm{RHi}_{max}$ represents the difference between the RHi_{max} value of ISSRs and the mean RHi of the horizontally adjacent (±∼ 230 m) subsaturated air. For both the ISSRs with and without the presence of ice crystals, H_2O variability is the dominant contributor to $d\mathrm{RHi}_{max}$ (Fig. 9). These results demonstrate that the strong contributions of H_2O heterogeneities to the spatial characteristics of ISSRs exist before, during and after ice nucleation, which suggests that the H_2O spatial heterogeneities are not just a result of ice crystal sedimentation and evaporation, but are already in place well before ice nucleation.

While H_2O spatial variabilities largely contribute to the horizontal characteristics of ISSRs, we also investigate the role of dynamics in determining the ISSR characteristics by analyzing the correlations between ISSRs and vertical wind velocity (w). We caution that the measurement of w during the in situ aircraft sampling is challenging, which may not capture the small scale turbulence well. Nevertheless, we assessed the correlations between the 1 Hz w variations and the ISS spatial variabilities. We define dw as the difference between the mean w value inside ISSRs and the mean w value of the horizontally adjacent (±∼ 230 m) subsaturated air. We apply the dw analyses to 785 ISSRs for which w data are reported. Of these ISSRs, 313 cases (∼ 40 %) are actually descending relative to their subsaturated environments, i.e., $dw<0$. In addition, we analyzed the dw values for the three types of ISSRs, as categorized in Fig. 7a. The results show that, compared with the adjacent non-ISSRs (±∼ 230 m), 40 %, 86 %, and 37 %, respectively, of ISSRs in types 1, 2, and 3 have descending motion relative to their surroundings ($dw<0$) (Fig. 10). To show that this result is not influenced by the scales of non-ISSRs being chosen for the dw calculation, various scales (from ±∼ 230 m to ±∼ 6.7 km) of non-ISSRs are tested. All results show a significant percentage (∼ 30–40 %) of ISSRs with relatively lower w than the non-ISSRs, regardless of the scales. Thus, while the air may be rising in general during the evolution of ISSRs in

Discussion Paper | Discussion Paper | Discussion Paper | Discussion Paper |

ACPD

13, 22249–22296, 2013

Cloud-scale ice supersaturated regions

M. Diao et al.

the larger spatial and temporal context (Spichtinger et al., 2005a, b), the microscale structure of ISSRs within the large scale uplift actually does not exactly correlate with the spatial variability of w in the Eulerian view.

4.4 Horizontal spatial variability of all RHi and the contributions from H_2O and T spatial variability

Because ISS ultimately derives from non-ISS (subsaturated and saturated) conditions, we further compare the RHi horizontal variabilities between ISS (Fig. 11a) and non-ISS (Fig. 11b) conditions. Based on Eq. (1), we analyze the contribution from H_2O and T to the horizontal RHi variabilities in terms of dRHi. Here dRHi represents the difference of the mean RHi values between one segment and its adjacent segment in the horizontal (dP<1 hPa). The analyses of 1 Hz dRHi show large contributions from H_2O horizontal variabilities for both ISS (0.93 ± 0.005) and non-ISS (0.94 ± 0.002) conditions. In addition, if we combine the ISS and non-ISS conditions and analyze the spatial variabilities of all RHi at 1 Hz scale (Fig. 12a), H_2O spatial variabilities contribute 0.93 ± 0.004 to the RHi variations.

To demonstrate that the contribution of H_2O spatial variability to dRHi is not an artifact of instrumental noise, we filtered the 1 Hz data with $|dH_2O\text{ppmv}|/H_2O\text{ppmv} \leq 3\,\%$. After removing these data, the contribution of H_2O horizontal variability to 1 Hz horizontal dRHi does not vary significantly, which is 0.96 ± 0.001. We note that the precision of the H_2O measurement is often $< 1\,\%$, which is much smaller than the criteria used here, so that we are likely removing real atmospheric fluctuations with this procedure. Similarly, when putting a very tight quality control on the precision of T measurement by filtering out the 1 Hz data with $|dT| \leq 0.1$ K, the contribution of H_2O horizontal variability to 1 Hz horizontal dRHi does not vary significantly either, which is 0.82 ± 0.003. Thus, even if the variabilities of H_2O and T well above the instrumental precision are filtered out, the H_2O horizontal variabilities always have large contributions to the RHi horizontal variabilities.

ACPD
13, 22249–22296, 2013

Another method of examining the RHi variabilities is to quantify the absolute deviation from a mean for both ISS and non-ISS conditions (see Eq. 3). Here σRHi represents the mean of the absolute differences between each 1 Hz RHi and the average RHi value within a certain horizontal segment. For example, at ~2.3 km scale, the σRHi analyses show that a ratio of 0.92 ± 0.001 of the 1 Hz RHi horizontal variabilities is contributed by the H_2O horizontal variabilities (Fig. 12b). To test whether our results hold for all cloud scales, various scales of dRHi and σRHi are chosen. From ~230 m up to ~115 km, the results all show much larger contributions from the H_2O horizontal variabilities (~0.9–0.8) to the RHi horizontal variabilities than from the T horizontal variabilities (~0.1–0.2) (Fig. 12c).

The above analyses of RHi spatial variability are restricted to $T \leq -40\,^{\circ}$C. To expand our analyses of RH spatial variability to various vertical levels, we binned the data by ranges of T (193–293 K, binned by 20 K), H_2O (0–10, 10–30, 30–100, 100–1000, >1000 ppmv) and P (<200 and 200–1000 hPa, binned by 200 hPa). We apply the dRHi analyses at 1 Hz scale to all the relative humidity (RH) observations from the surface to the UT/LS. The results in Table 1 show that the H_2O horizontal variabilities always have dominant contributions to RH horizontal variabilities, and these H_2O contributions decrease slightly from the surface to the UT/LS, e.g., from 0.94 ± 0.001 at >800 hPa to 0.90 ± 0.001 at 0–200 hPa. Although not shown in Table 1, the standard deviations of all the $d\mathrm{RHi}_T$ and $d\mathrm{RHi}_q$ values are smaller than the last digit of these fits. This finding is consistent with the previous findings about the decreasing variances of H_2O concentrations from the surface to the UT region (Cho et al., 2000; Kahn and Teixeira, 2009; Kahn et al., 2011).

4.5 Dynamical conditions of ISS with tracer-tracer correlation analyses

To understand the scales of the dynamics that influence the formation of ISSRs, we examine two independent pairs of conservative tracers in extratropical regions, that is, the O_3-CO correlation (Pan et al., 2004) and the total water content (H_2O_{tot})-wet equivalent potential temperature (θ_q) correlation (Paluch, 1979). Here total water mass mixing ratio is calculated by combining the VCSEL water vapor mass mixing ratio with ice water content measured by the CU laser hygrometer (Davis et al., 2007). The θ_q values are calculated based on the equations given in Appendix A1. For both tracer-tracer correlations in Fig. 13, the grey background points represent all observations including both ISS and non-ISS, while the colored markers represent ISS observations with each type of marker representing one flight. In general, the values of tracer correlations should remain constant (i.e., a single point in the correlation plot) if air parcels are sampled from the same origin (i.e., same chemical tracer values). Otherwise, if mixing between air parcels from different origins has occurred, the correlation between the tracers follows a line or curve.

The O_3-CO correlation can be used to highlight stratospheric-tropospheric mixing. According to Pan et al. (2004), we define the chemical tropospheric and stratospheric regions based on the O_3-CO correlations in START08. The chemical troposphere is defined by the linear fit to O_3<70 ppbv, that is, $y = a + b \times x$, where y is O_3 (ppbv), and x is CO (ppbv). Here a is 47.0 ± 0.1, b is 0.063 ± 0.010, and the standard deviation of the residuals (σ_y) is 10.5. In Fig. 13a, the linear fit and $\pm 3\ \sigma_y$ of the fit are shown as the black line and red dotted lines, respectively. Below the upper red dotted line is the chemical troposphere, and above is the troposphere-stratosphere transition layer (Pan et al., 2004). The results show that most of the ISS observations (colored markers) from individual flights follow almost straight mixing lines. The extrapolations of these mixing lines can help determine the origins of air parcels being mixed. For example, the O_3-CO mixing lines with positive slopes represent tropospheric-tropospheric mixing (RF09, 16, 17 in Fig. 13a), since the extrapolations of the mixing lines intercept tropospheric air at the two ends. On the other hand, the mixing lines with negative slopes represent stratospheric-tropospheric mixing (RF11, 15 in Fig. 13A), since their extrapolations intercept stratospheric air at one end and tropospheric air at the other (such as discussed in Zahn et al., 2004).

The O_3-CO correlation captures the stratospheric-tropospheric mixing well, but to highlight the tropospheric-tropospheric mixing, $H_2O_{tot} - \theta_q$ correlation is also analyzed

ACPD
13, 22249–22296, 2013

here. In general, the background of the atmosphere from the surface to the UT/LS is represented as a "C" shape in the $H_2O_{tot} - \theta_q$ correlation (i.e., the grey background in Fig. 13b). The combination of high H_2O_{tot} and low θ_q values (upper left region) represent the tropospheric region, while the combination of low H_2O_{tot} and high θ_q values (lower right region) represent the stratospheric region. Compared with the ISS distributions in O_3-CO correlation, the ISS distributions in $H_2O_{tot} - \theta_q$ correlation (colored markers in Fig. 13b) follow mixing lines that deviate slightly from the straight mixing lines, which imply that the specific entropy of the air is not fully conserved. For example, if irreversible processes happen, including external inputs of sensible and/or latent heating and precipitation, the mixing lines would deviate from a straight line. Based on the extrapolations of the observed mixing lines, negative and positive slopes represent tropospheric-tropospheric (RF09, 16, 17 in Fig. 13b) and stratospheric-tropospheric (RF11, 15 in Fig. 13b) mixing, respectively.

Most ISS mixing lines are straight, and their end points are far apart from each other, which indicate that the formation of ISS involves the mixing of two distinctively different types of air parcels (see Appendix A2). This feature could be explained by the previous findings that large scale uplift usually plays an important role in ISSR formation (Spichtinger et al., 2005a, b). The evenly distributed points along the mixing lines show that the air parcels have been well mixed on the small scale, since otherwise clusters of points would be observed at the two end points. This result is consistent with the previous simulation which shows that small scale turbulence and eddies play important roles in triggering ISS formation and the subsequent ice freezing events (Fusina and Spichtinger, 2010). Thus, both large- and small-scale processes play important roles in setting the environment of ISSR formation. On the one hand, uplifting and cooling provide the environments for ISSR formation on the mesoscale, and contribute to the increase of RHi in the Lagrangian view (Spichtinger et al., 2005a, b). On the other hand, the small-scale processes contribute to the microscale structure of ISSRs, which agree with the widely observed turbulence in the troposphere (Gage and Nastrom, 1986; Nastrom and Gage, 1985; Nastrom et al., 1986), and also explain that H_2O

ACPD
13, 22249–22296, 2013

Cloud-scale ice supersaturated regions

M. Diao et al.

spatial variabilities instead of T spatial variabilities largely contribute to the RHi spatial variabilities on the microscale. We caution that measurements of 3-D wind fields are needed to fully understand the microscale dynamics of ISSR formation, and the exact causal relationship along the evolution history of the ISSRs needs more investigation in the future.

4.6 Eulerian view examples of using H_2O and T variabilities to derive RHi variabilities

Here we use one example to demonstrate that the importance of H_2O horizontal variabilities when deriving the RHi horizontal variabilities in the Eulerian view (Fig. 14). Figure 14a shows the typical time series of RHi during a flight. If one only uses T spatial fluctuations at one point in time to derive RHi spatial variability and neglect the H_2O spatial fluctuations (Fig. 14b red short dashed line), the generated ISS occurrences (Fig. 14b) would be much lower compared with those in real observations (Fig. 14a). In addition, if one uses T fluctuations to compensate for the neglected H_2O fluctuations, even though the RHi field is the same, the generated T in ISSRs would be unnecessarily much lower (by ~ 2 K, Fig. 14c) than the observed T in ISSRs (Fig. 14a). The artificially lower T inside the ISSRs in this case will lead to unrealistic conditions for ice nucleation, given the sensitivities of ice crystal growth rate and small scale turbulences to the T field. Thus it is critical that the spatial variabilities of H_2O are considered instead of being neglected or compensated by T spatial variabilities. The extent of H_2O horizontal variabilities may be a useful observational constraint to compare the 4-D cloud microphysics models with 1-D aircraft observations.

5 Atmospheric implications and future work

The causes of microscale H_2O spatial variabilities likely are attributed to many dynamical processes; for example, small scale turbulence, gravity wave, entrainment mixing,

ACPD
13, 22249–22296, 2013

etc. Since current back trajectories of air parcels cannot fully account for the dynamical processes on the microscale, it is impossible to determine the individual causes of these observed small-scale H_2O variabilities. However, our results show that although the dynamic causes of H_2O variabilities may differ, the strong correlation between RHi and H_2O horizontal variabilities holds at each horizontal layer from the surface to the extratropical UT/LS and tropical UT, from 87° N to 67° S, and is applicable for all cloud scales. We note that our analyses are limited to the Eulerian view correlations between the spatial variabilities of H_2O, T and RHi, since in the Lagrangian view, the changes of T and w in time may be the main influences on the temporal variability of RHi. However, given that in situ observations of the true Lagrangian view are very difficult to obtain, this work provides the first step to understand the microscale structure of ISSRs and its correlation with spatial heterogeneities of H_2O, T, and w in the Eulerian view.

The strong spatial correlations between ISSRs and high H_2O heterogeneities are ubiquitously observed in this work, which provide a unique validation method for cloud and climate models on ISS spatial variability. In particular, currently there are various small-scale dynamics considered in the cloud models (Jensen and Pfister, 2004; Spichtinger and Krämer, 2012), as well as various parameterization schemes used to generate ISS sub-grid variability in the climate models (Kärcher and Burkhardt, 2008; Wang and Penner, 2010). Recent results from some cirrus cloud models showed that including the ISS generated by small-scale dynamical processes can have large impacts on cloud microphysics and ice crystal properties (Jensen and Pfister, 2004; Spichtinger and Krämer, 2012). Climate models also showed that the inclusion of sub-grid scale ISS variability can modify the cloud radiative forcing on the atmosphere (Kärcher and Burkhardt, 2008; Wang and Penner, 2010). In fact, most cloud models (Jensen and Pfister, 2004; Jensen, 2005) and climate models (Kärcher and Burkhardt, 2008; Wang and Penner, 2010) have been using T variability as one of the main constraints for ISS variability, because not only it is commonly accepted that the decrease of T drives the increase of RHi in a mass-conservative Lagrangian view, but also it is known that the mesoscale (~ 100's km) T fluctuations have been widely observed in the UT/LS (Gary, 2006). Future work is needed to compare the simulation results with the observations on the contribution of H_2O spatial variability to RHi spatial variability in each horizontal layer. Understanding how the spatial H_2O variability comes about, and why it is such a dominant factor in the Eulerian view RHi field, will require future modeling studies and ultimately more accurate cloud models.

Appendix A

A1 Calculation of wet equivalent potential temperature (θ_q)

We here show the derivation of θ_q that has been used in our analyses. At $T \leq -40\,^{\circ}\mathrm{C}$, air parcels contain dry air, water vapor and ice particles with no supercooled liquid water (Murphy and Koop, 2005). The entropy of air can be expressed as:

$$s = s_\mathrm{d} + q s_\mathrm{v} + r_\mathrm{ice} s_\mathrm{ice}, \tag{A1}$$

where s_d, s_v and s_ice are the specific entropy of dry air, water vapor and ice, respectively. q and r_ice are the mass mixing ratios of water vapor and ice ($\mathrm{kg\,kg^{-1}}$), respectively.

$$s_\mathrm{d} = C_\mathrm{pd} \ln T - R_\mathrm{d} \ln P_\mathrm{d}, \tag{A2}$$

$$s_\mathrm{v} = C_\mathrm{pv} \ln T - R_\mathrm{v} \ln e, \tag{A3}$$

$$s_\mathrm{ice} = C_\mathrm{ice} \ln T, \tag{A4}$$

where R_d ($287\,\mathrm{J\,kg^{-1}\,K^{-1}}$) and R_v ($461\,\mathrm{J\,kg^{-1}\,K^{-1}}$) are the gas constants for dry air and water vapor, respectively (Emanuel, 1994). P_d and e are dry air and water vapor

ACPD
13, 22249–22296, 2013

partial pressures (Pa), respectively. C_{pd} (1004 J kg^{-1} K^{-1}), C_{pv} (1870 J kg^{-1} K^{-1}) and C_{ice} (J kg^{-1} K^{-1}) are the specific heats of dry air at constant pressure, water vapor at constant pressure and ice, respectively (Emanuel, 1994). C_{ice} is calculated based on the value of molecular heat capacity of ice ($C_{p,ice}$). Here the calculation of $C_{p,ice}$ at T>20 K is shown as below (Emanuel, 1994; Giauque and Stout, 1936):

$$C_{p,ice} = -2.0572 + 0.14644T + 0.06163T\exp\left(-\left(\frac{T}{125.1}\right)^2\right), \tag{A5}$$

where T is temperature in K and $C_{p,ice}$ is in J kg^{-1} K^{-1}. We use $T = -51.8\,^{\circ}$C (mean temperature in START08) and get $C_{p,ice}$ = 31.0 J mol^{-1} K^{-1}, thus C_{ice} = 1.75 × 10^3 J kg^{-1} K^{-1}.

Based on the definition of wet equivalent potential temperature (θ_q) in Emanuel (1994) Eq. (4.5.11) for warm clouds (mixture of liquid water droplets, water vapor and dry air), we derive our θ_q for cold clouds (mixture of ice particles, water vapor and dry air at $T \leq -40\,^{\circ}$C). Our calculation of θ_q is shown as below and it applies to the entire RHi range from subsaturation to supersaturation:

$$\theta_q = T\left(\frac{p_0}{p_d}\right)^{\frac{R_d}{C_{pd}+QC_{ice}}}\left(\frac{\mathrm{RHi}}{100}\right)^{-\frac{qR_v}{C_{pd}+QC_{ice}}}\exp\left(\frac{L_{ice}q}{(C_{pd}+QC_{ice})T}\right), \tag{A6}$$

where P_0 is the reference pressure of 1000 mb; the total water content Q is defined as $Q = q + r_{ice}$; L_{ice} is the latent heat of sublimation. The function of L_{ice} for T>30 K is as below (Murphy and Koop, 2005):

$$L_{ice} = 46782.5 + 35.8925T - 0.07414T^2 + 541.5\exp\left(-\left(\frac{T}{123.75}\right)^2\right), \tag{A7}$$

where T is temperature in K. We use $T = -51.8\,^{\circ}$C (mean temperature in START08) and get L_{ice} = 5.11 × 10^4 J mol^{-1} K^{-1}, thus L_{ice} = 2.84 × 10^6 J kg^{-1} K^{-1}. Equation (A6) applies for all conditions: subsaturation, saturation and supersaturation as well as both clear-sky and in-cloud conditions.

ACPD
13, 22249–22296, 2013

A2 Mixing line mechanism

Chemical tracers inside the parcels can be considered to be conservative tracers if they have much longer lifetimes than the mixing time scale. For example, O_3 and CO can be used as tracers of tropospheric and stratospheric air, respectively. If the research aircraft samples through a region that contains air parcels from very different origins, this mixing feature will show up in the tracer-tracer correlation plot as a curve or line, which means that the concentrations of conservative properties show variations along the sampling transect. If there is no mixing process, the correlation plot should show almost the same values throughout. Whether the mixing feature will appear as a curve or a straight line in the correlation plots is determined by the number of different levels of air that are mixed altogether. The straight line represents mixing of air parcels only from two levels, while the curve represents mixing of air from more than two levels (Paluch, 1979). In the case of mixing of two levels, we use X and Y to represent the two conservative properties, and subscripts 1 and 2 to represent two air parcels. The conserved properties after mixing (X' and Y') can be calculated as:

$$X' = f_1 X_1 + f_2 X_2,$$

$$Y' = f_1 Y_1 + f_2 Y_2,$$

where f_1 and f_2 are the fractions of a unit mass of the final mixture constituted by fluid originally contained by parcel 1 and 2, respectively. By mass conservation, $f_1 + f_2 = 1$. The ratio of the two conserved properties X and Y after mixing follows a certain relationship as below:

$$Y' = X' \frac{Y_2 - Y_1}{X_2 - X_1} + Y_1 - \frac{X_1(Y_2 - Y_1)}{X_2 - X_1}.$$

The correlation of $Y(X)$ has a constant slope, $\frac{Y_2 - Y_1}{X_2 - X_1}$, which is only defined by the initial values of X_1, X_2, Y_1 and Y_2. The intercept of the correlation is $Y_1 - \frac{X_1(Y_2 - Y_1)}{X_2 - X_1}$, which

ACPD
13, 22249–22296, 2013
Cloud-scale ice supersaturated regions
M. Diao et al.

is also a constant. The values of the conservative properties along the straight mixing line are bounded by the original values at the two levels. Therefore, by extrapolating the mixing lines the origins of the mixed air can be coarsely estimated (Paluch, 1979; Pan et al., 2004).

To demonstrate that the mixing between more than two levels would not follow a straight line, we show the example of three-level mixing. Here X and Y still represent the two conservative properties and subscripts 1, 2 and 3 represent three air parcels, then the conserved properties after mixing (X' and Y') can be calculated as:

$$X' = f_1 X_1 + f_2 X_2 + f_3 X_3,$$

$$Y' = f_1 Y_1 + f_2 Y_2 + f_3 Y_3,$$

where f_1, f_2 and f_3 are the fractions of a unit mass of the final mixture constituted by fluid originally contained by parcels 1, 2 and 3, respectively. By mass conservation, $f_1 + f_2 + f_3 = 1$. In this case there are five variables (X, Y, f_1, f_2 and f_3) in three equations. Therefore Y is not only a function of X but also depends on the ratio of the mixing. The function of $Y(X, f_3)$ is shown as below (similar functions can be derived for $Y(X, f_1)$ and $Y(X, f_2)$):

$$Y' = X' \frac{Y_2 - Y_1}{X_2 - X_1} + f_3 \left(Y_3 - Y_1 - \frac{(Y_2 - Y_1)(X_3 - X_1)}{(X_2 - X_1)}\right) + Y_1 - \frac{X_1 (Y_2 - Y_1)}{X_2 - X_1}.$$

The $Y(X, f_3)$ correlation function will not follow a straight line in the correlation plot since it is highly unlikely that f_3 (or f_1, f_2) will be constant within the mixing region as the mixing inside the region is not strictly uniform everywhere.

Acknowledgements. We gratefully acknowledge funding for field support and data analyses from the following sources: NSF ATM-0840732 (HIPPO Global campaign) and AGS-1036275 (START08 campaign) for VCSEL (Princeton). M. Diao gratefully acknowledges support from the NASA Earth and Space Science Graduate Fellowship (NASA NNX09AO51H) and the Walbridge Fund Graduate Award. We appreciate the efforts of NCAR EOL flight, technical, and

ACPD
13, 22249–22296, 2013

mechanical crews during START08 and HIPPO1, in particular, P. Romashkin for field maintenance of the VCSEL hygrometer. We also appreciate helpful discussions with L. Donner, S. Fueglistaler, L. L. Pan and I. M. Held.

References

Cho, J. Y. N., Newell, R. E., and Sachse, G. W.: Anomalous scaling of mesoscale tropospheric humidity fluctuations, Geophys. Res. Lett., 27, 377–380, doi:10.1029/1999GL010846, 2000.

Cotton, R., Osborne, S., Ulanowski, Z., Hirst, E., Kaye, P. H., and Greenaway, R. S.: The Ability of the Small Ice Detector (SID-2) to Characterize Cloud Particle and Aerosol Morphologies Obtained during Flights of the FAAM BAe-146 Research Aircraft, J. Atmos. Ocean. Tech., 27, 290–303, doi:10.1175/2009JTECHA1282.1, 2010.

Cziczo, D. J., Froyd, K. D., Hoose, C., Jensen, E. J., Diao, M., Zondlo, M. A., Smith, J. B., Twohy, C. H., and Murphy, D. M.: Clarifying the Dominant Sources and Mechanisms of Cirrus Cloud Formation, Science, 340, 1320–1324, doi:10.1126/science.1234145, 2013.

Davis, S. M., Hallar, A. G., Avallone, L. M., and Engblom, W.: Measurement of total water with a tunable diode laser hygrometer: Inlet analysis, calibration procedure, and ice water content determination, J. Atmos. Ocean. Tech., 24, 463–475, doi:10.1175/JTECH1975.1, 2007.

Diao, M., Zondlo, M. A., Heymsfield, A. J., Beaton, S. P., and Rogers, D. C.: Evolution of ice crystal regions on the microscale based on in situ observations, Geophys. Res. Lett., 40, 3473–3478, doi:10.1002/grl.50665, 2013.

Dickson, N. C., Gierens, K. M., Rogers, H. L., and Jones, R. L.: Probabilistic description of ice-supersaturated layers in low resolution profiles of relative humidity, Atmos. Chem. Phys., 10, 6749–6763, doi:10.5194/acp-10-6749-2010, 2010.

Emanuel, K. A.: Atmospheric Convection, Oxford University Press., 1994.

Fusina, F. and Spichtinger, P.: Cirrus clouds triggered by radiation, a multiscale phenomenon, Atmos. Chem. Phys., 10, 5179–5190, doi:10.5194/acp-10-5179-2010, 2010.

Gage, K. S. and Nastrom, G. D.: Theoretical Interpretation of Atmospheric Wavenumber Spectra of Wind and Temperature Observed by Commercial Aircraft During GASP, J. Atmos. Sci., 43, 729–740, doi:10.1175/1520-0469(1986)043<0729:TIOAWS>2.0.CO;2, 1986.

Gary, B. L.: Mesoscale temperature fluctuations in the stratosphere, Atmos. Chem. Phys., 6, 4577–4589, doi:10.5194/acp-6-4577-2006, 2006.

ACPD
13, 22249–22296, 2013

Gettelman, A., Fetzer, E. J., Eldering, A., and Irion, F. W.: The Global Distribution of Supersaturation in the Upper Troposphere from the Atmospheric Infrared Sounder, J. Climate, 19, 6089–6103, doi:10.1175/JCLI3955.1, 2006.

Giauque, W. F. and Stout, J. W.: The entropy of water and the third law of thermodynamics. The heat capacity of ice from 15 to 274 ° K, J. Am. Chem. Soc., 58, 1144–1150, 1936.

Gierens, K., Kohlhepp, R., Dotzek, N., and Smit, H. G.: Instantaneous fluctuations of temperature and moisture in the upper troposphere and tropopause region. Part 1: Probability densities and their variability, Meteorol. Z., 16, 221–231, doi:10.1127/0941-2948/2007/0197, 2007.

Gierens, K. and Spichtinger, P.: On the size distribution of ice-supersaturated regions in the upper troposphere and lowermost stratosphere, Ann. Geophys., 18, 499–504, doi:10.1007/s00585-000-0499-7, 2000.

Heintzenberg, J. and Charlson, R. J.: Clouds in the Perturbed Climate System: Their Relationship to Energy Balance, Atmospheric Dynamics, and Precipitation, edited by J. Heintzenberg and J. R. Charlson, MIT Press, Cambridge, Mass., 2009.

Heymsfield, A. J., Miloshevich, L. M., Twohy, C., Sachse, G., and Oltmans, S.: Upper-tropospheric relative humidity observations and implications for cirrus ice nucleation, Geophys. Res. Lett., 25, 1343, doi:10.1029/98GL01089, 1998.

Jensen, E. J.: Formation of a tropopause cirrus layer observed over Florida during CRYSTAL-FACE, J. Geophys. Res., 110, D03208, doi:10.1029/2004JD004671, 2005.

Jensen, E. J. and Pfister, L.: Transport and freeze-drying in the tropical tropopause layer, J. Geophys. Res., 109, D02207, doi:10.1029/2003JD004022, 2004.

Kahn, B. H. and Teixeira, J.: A Global Climatology of Temperature and Water Vapor Variance Scaling from the Atmospheric Infrared Sounder, J. Climate, 22, 5558–5576, doi:10.1175/2009JCLI2934.1, 2009.

Kahn, B. H., Gettelman, A., Fetzer, E. J., Eldering, A., and Liang, C. K.: Cloudy and clear-sky relative humidity in the upper troposphere observed by the A-train, J. Geophys. Res., 114, D00H02, doi:10.1029/2009JD011738, 2009.

Kahn, B. H., Teixeira, J., Fetzer, E. J., Gettelman, A., Hristova-Veleva, S. M., Huang, X., Kochanski, A. K., Köhler, M., Krueger, S. K., Wood, R., and Zhao, M.: Temperature and Water Vapor Variance Scaling in Global Models: Comparisons to Satellite and Aircraft Data, J. Atmos. Sci., 68, 2156–2168, doi:10.1175/2011JAS3737.1, 2011.

Kärcher, B. and Burkhardt, U.: A cirrus cloud scheme for general circulation models, Q. J. Roy. Meteorol. Soc., 134, 1439–1461, doi:10.1002/qj.301, 2008.

Koop, T., Luo, B., Tsias, A., and Peter, T.: Water activity as the determinant for homogeneous ice nucleation in aqueous solutions, Nature, 406, 611–4, doi:10.1038/35020537, 2000.

Korolev, A. V., Emery, E. F., Strapp, J. W., Cober, S. G., Isaac, G. A., Wasey, M., and Marcotte, D.: Small Ice Particles in Tropospheric Clouds: Fact or Artifact? Airborne Icing Instrumentation Evaluation Experiment, B. Am. Meteorol. Soc., 92, 967–973, doi:10.1175/2010BAMS3141.1, 2011.

Krämer, M., Schiller, C., Afchine, A., Bauer, R., Gensch, I., Mangold, A., Schlicht, S., Spelten, N., Sitnikov, N., Borrmann, S., de Reus, M., and Spichtinger, P.: Ice supersaturations and cirrus cloud crystal numbers, Atmos. Chem. Phys., 9, 3505–3522, doi:10.5194/acp-9-3505-2009, 2009.

Lamquin, N., Stubenrauch, C. J., Gierens, K., Burkhardt, U., and Smit, H.: A global climatology of upper-tropospheric ice supersaturation occurrence inferred from the Atmospheric Infrared Sounder calibrated by MOZAIC, Atmos. Chem. Phys., 12, 381–405, doi:10.5194/acp-12-381-2012, 2012.

Liou, K. N.: Radiation and cloud processes in the atmosphere, Oxford University Press., 1992.

Lynch, D. K., Sassen, K., Starr, D. C., and Stephens, G.: Cirrus, edited by D. K. Lynch, K. Sassen, D. C. Starr, and G. Stephens, Oxford Univ. Press, New York, 2002.

Murphy, D. M. and Koop, T.: Review of the vapour pressures of ice and supercooled water for atmospheric applications, Q. J. Roy. Meteorol. Soc., 131, 1539–1565, doi:10.1256/qj.04.94, 2005.

Nastrom, G. D. and Gage, K. S.: A Climatology of Atmospheric Wavenumber Spectra of Wind and Temperature Observed by Commercial Aircraft, J. Atmos. Sci., 42(9), 950–960, doi:10.1175/1520-0469(1985)042<0950:ACOAWS>2.0.CO;2, 1985.

Nastrom, G. D., Jasperson, W. H., and Gage, K. S.: Horizontal spectra of atmospheric tracers measured during the Global Atmospheric Sampling Program, J. Geophys. Res., 91, 13201–13209, doi:10.1029/JD091iD12p13201, 1986.

Ovarlez, J., Gayet, J. F., Gierens, K., Strom, J., Ovarlez, H., Auriol, F., Busen, R., and Schumann, U.: Water vapour measurements inside cirrus clouds in Northern and Southern hemispheres during INCA, Geophys. Res. Lett., 29, 1813, doi:10.1029/2001GL014440, 2002.

Paluch, I. R.: The Entrainment Mechanism in Colorado Cumuli, J. Atmos. Sci., 36, 2467–2478, 1979.

Pan, L. L., Randel, W. J., Gary, B. L., Mahoney, M. J., and Hintsa, E. J.: Definitions and sharpness of the extratropical tropopause: A trace gas perspective, J. Geophys. Res., 109, D23103, doi:10.1029/2004JD004982, 2004.

Pan, L. L., Bowman, K. P., Atlas, E. L., Wofsy, S. C., Zhang, F., Bresch, J. F., Ridley, B. A., Pittman, J. V., Homeyer, C. R., Romashkin, P., and Cooper, W. A.: The Stratosphere–Troposphere Analyses of Regional Transport 2008 Experiment, B. Am. Meteorol. Soc., 91, 327–342, doi:10.1175/2009BAMS2865.1, 2010.

Peter, T., Marcolli, C., Spichtinger, P., Corti, T., Baker, M. B., and Koop, T.: When dry air is too humid, Science, 314, 1399–402, doi:10.1126/science.1135199, 2006.

Price, J. D. and Wood, R.: Comparison of probability density functions for total specific humidity and saturation deficit humidity,and consequences for cloud parametrization, Q. J. Roy. Meteorol. Soc., 128, 2059–2072, doi:10.1256/003590002320603539, 2002.

Solomon, S., Qin, D., Manning, M., Chen, Z., Marquis, M., Avery, K. B., Tignor, M., and Miller, H. L.: Climate Change 2007: The Physical Science Basis, edited by: Solomon, S., Qin, D., Manning, M., Chen, Z., Marquis, M., Avery, K. B., Tignor, M., and Miller, H. L., Cambridge University Press, 2007.

Spichtinger, P. and Krämer, M.: Tropical tropopause ice clouds: a dynamic approach to the mystery of low crystal numbers, Atmos. Chem. Phys. Discuss., 12, 28109–28153, doi:10.5194/acpd-12-28109-2012, 2012.

Spichtinger, P., Gierens, K., and Read, W.: The global distribution of ice-supersaturated regions as seen by the Microwave Limb Sounder, Q. J. Roy. Meteorol. Soc., 129, 3391–3410, doi:10.1256/qj.02.141, 2003.

Spichtinger, P., Gierens, K., and Dörnbrack, A.: Formation of ice supersaturation by mesoscale gravity waves, Atmos. Chem. Phys., 5, 1243–1255, doi:10.5194/acp-5-1243-2005, 2005a.

Spichtinger, P., Gierens, K., and Wernli, H.: A case study on the formation and evolution of ice supersaturation in the vicinity of a warm conveyor belt's outflow region, Atmos. Chem. Phys., 5, 973–987, doi:10.5194/acp-5-973-2005, 2005b.

Tilmes, S., Pan, L. L., Hoor, P., Atlas, E., Avery, M. A., Campos, T., Christensen, L. E., Diskin, G. S., Gao, R. S., Herman, R. L., Hintsa, E. J., Loewenstein, M., Lopez, J., Paige, M. E., Pittman, J. V, Podolske, J. R., Proffitt, M. R., Sachse, G. W., Schiller, C., Schlager, H., Smith, J., Spelten, N., Webster, C., Weinheimer, A. and Zondlo, M. A.: An aircraft-based upper troposphere lower stratosphere O_3, CO, and H_2O climatology for the Northern Hemisphere, J. Geophys. Res., 115, D14303, doi:10.1029/2009JD012731, 2010.

ACPD
13, 22249–22296, 2013

Cloud-scale ice supersaturated regions

M. Diao et al.

Vömel, H., Oltmans, S. J., Johnson, B. J., Hasebe, F., Shiotani, M., Fujiwara, M., Nishi, N., Agama, M., Cornejo, J., Paredes, F., and Enriquez, H.: Balloon-borne observations of water vapor and ozone in the tropical upper troposphere and lower stratosphere, J. Geophys. Res., 107, 8–16, doi:10.1029/2001JD000707, 2002.
Wang, M. and Penner, J. E.: Cirrus clouds in a global climate model with a statistical cirrus cloud scheme, Atmos. Chem. Phys., 10, 5449–5474, doi:10.5194/acp-10-5449-2010, 2010.
Wofsy, S. C., Daube, B. C., Jimenez, R., Kort, E., Pittman, J. V., Park, S., Commane, R., Xiang, B., G.Santoni, Jacob, D., Fisher, J., Pickett-Heaps, C., Wang, H., Wecht, K., Wang, Q.-Q., Stephens, B. B., Schertz, S., Romashkin, P., Campos, T., Haggerty, J., Cooper, W. A., Rogers, D., Beaton, S., Elkins, J. W., Fahey, D., Gao, R., Moore, F., Montzka, S. A., Schwartz, J. P., Hurst, D., Miller, B., Sweeney, C., Oltmans, S., Nance, D., Hintsa, E. F., Dutton, G., Watts, L. A., Spackman, R., Rosenlof, K., Ray, E., Zondlo, M. A., Diao, M., Mahoney, M. J., Chahine, M. T., Olsen, E., Keeling, R., Bent, J., Atlas, E. A., Lueb, R., Patra, P., Ishijima, K., Engelen, R., Nassar, R., Jones, D. B., and Mikaloff-Fletcher., S.: HIAPER Pole-to-Pole Observations (HIPPO): fine-grained, global-scale measurements of climatically important atmospheric gases and aerosols, Philosophical transactions of the Royal Society. Series A, Mathematical, physical, and engineering sciences, 369, 2073–2086, doi:10.1098/rsta.2010.0313, 2011.
Wood, R. and Field, P. R.: The Distribution of Cloud Horizontal Sizes, J. Climate, 24, 4800–4816, doi:10.1175/2011JCLI4056.1, 2011.
Wylie, D. P. and Menzel, W. P.: Eight Years of High Cloud Statistics Using HIRS, J. Climate, 12, 170–184, doi:10.1175/1520-0442-12.1.170, 1999.
Zahn, A., Brenninkmeijer, C. A. M., and van Velthoven, P. F. J.: Passenger aircraft project CARIBIC 1997–2002, Part I: the extratropical chemical tropopause, Atmos. Chem. Phys. Discuss., 4, 1091–1117, doi:10.5194/acpd-4-1091-2004, 2004.
Zondlo, M. A., Paige, M. E., Massick, S. M., and Silver, J. A.: Vertical cavity laser hygrometer for the National Science Foundation Gulfstream-V aircraft, J. Geophys. Res., 115, D20309, doi:10.1029/2010JD014445, 2010.

ACPD
13, 22249–22296, 2013

Table 1. Contributions of H_2O and T horizontal variabilities to RH horizontal variabilities at various T, H_2O and P ranges.

Bin by H_2O			Bin by T			Bin by P		
H_2O (ppmv)	$d\mathrm{RHi}_q$	$d\mathrm{RHi}_T$	T(°C)	$d\mathrm{RHi}_q$	$d\mathrm{RHi}_T$	P(hPa)	$d\mathrm{RHi}_q$	$d\mathrm{RHi}_T$
0–10	0.73	0.27	−80–−60	0.88	0.12	0–200	0.90	0.097
10–30	0.89	0.11	−60–−40	0.94	0.062	200–400	0.96	0.042
30–100	0.90	0.10	−40–−20	0.98	0.024	400–600	0.97	0.027
100–1000	0.95	0.046	−20–0	0.97	0.035	600–800	0.96	0.041
> 1000	0.96	0.038	> 0	0.94	0.059	> 800	0.94	0.061

ACPD
13, 22249–22296, 2013

Title Page
Abstract
Introduction
Conclusions
References
Tables
Figures
◀I
▶I
◀
▶
Back
Close
Full Screen / Esc
Printer-friendly Version
Interactive Discussion

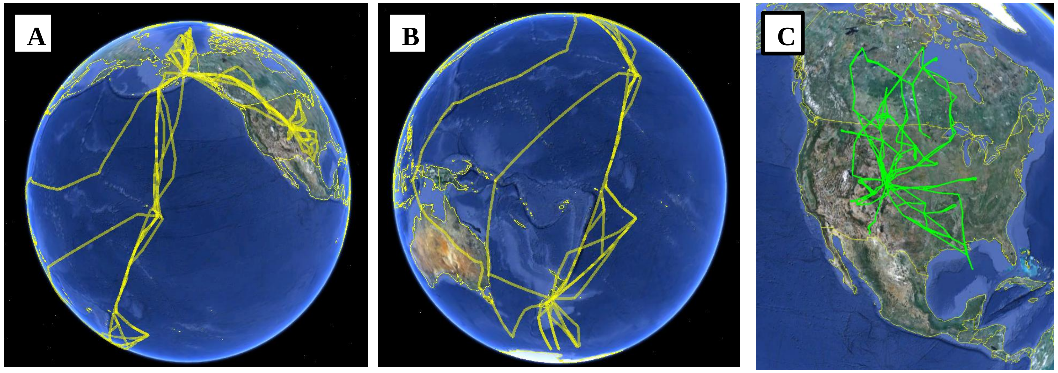

Fig. 1. Google map of START08 and HIPPO flights analyzed in this study. Yellow lines represent flight tracks of HIPPO#1–5 campaign and green lines represent the flight tracks of Research Flights 4–18 (RF04–RF18) in START08.

ACPD
13, 22249–22296, 2013

Title Page
Abstract | Introduction
Conclusions | References
Tables | Figures
◀◀ | ▶▶
◀ | ▶
Back | Close
Full Screen / Esc
Printer-friendly Version
Interactive Discussion

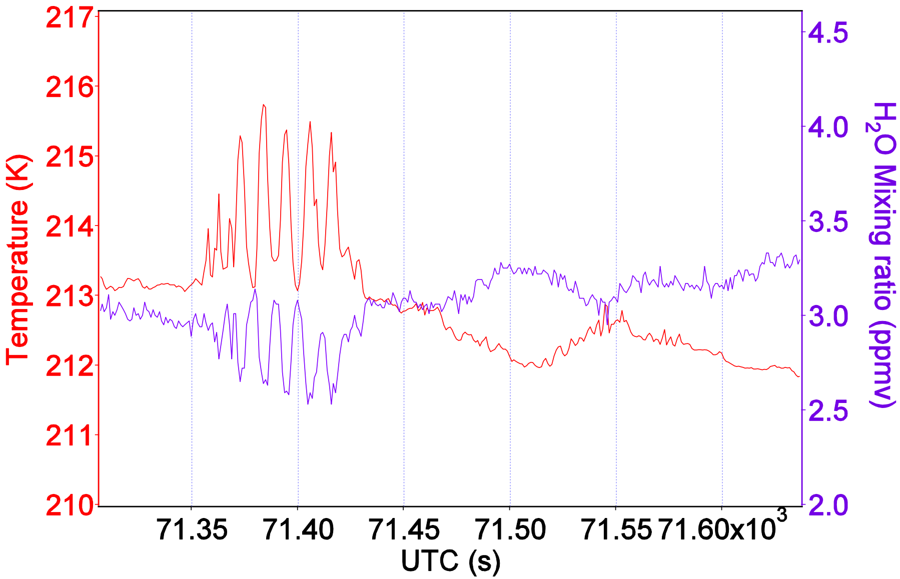

Fig. 2. In-flight synchronization between temperature (T) and water vapor (H_2O) measurements. Fluctuations in T (red) and H_2O (purple) due to a gravity wave were observed during RF08 of START08. These fast fluctuations demonstrate the accurate synchronization of T and H_2O measurements at the 1 Hz timescale.

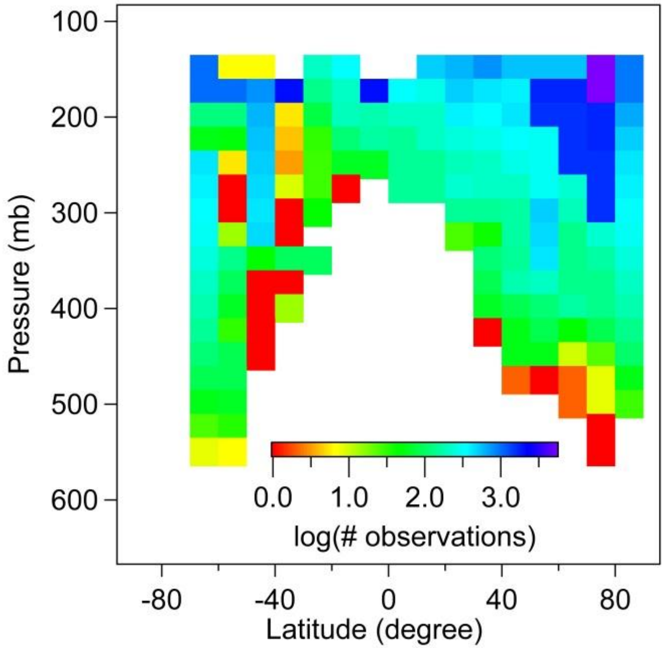

Fig. 3. Distribution of the number of observations at $T \leq -40\,^{\circ}\mathrm{C}$ in the latitudinal and vertical view for the START08 and HIPPO campaigns. The color code shows the number of observations in each $10^{\circ} \times 25$ mb bin in the log scale.

ACPD
13, 22249–22296, 2013

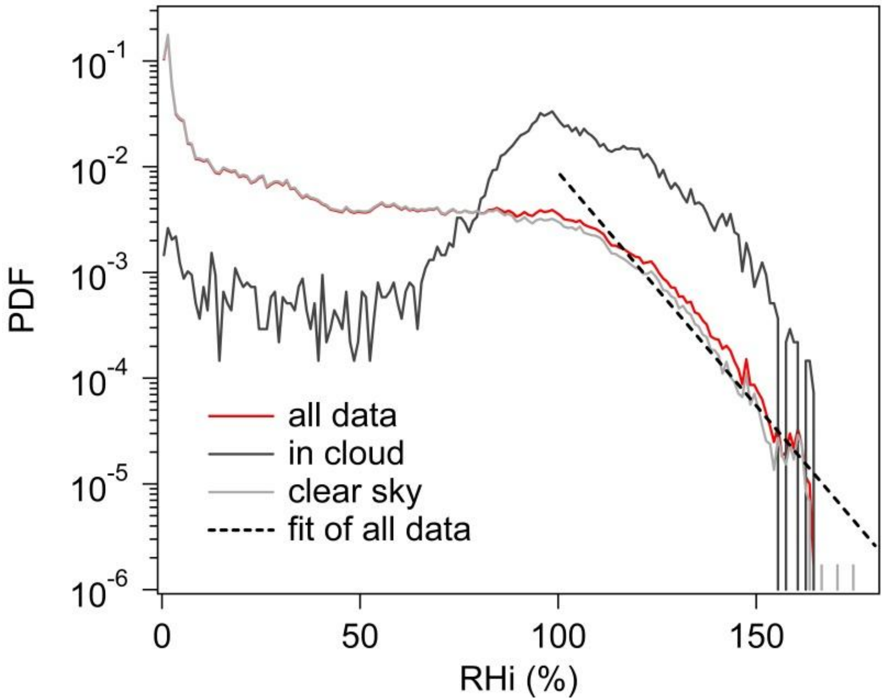

Fig. 4. PDFs of RHi for 1 Hz START08 and HIPPO#2–5 data. Different colors represent RHi of all data (red), the clear-sky (light grey) and the in-cloud data (dark grey). For all the 1 Hz data (red), the PDF of RHi > 100 % follows an exponential decay: ln(PDF) = $a + b \times$ RHi, where a = 5.4 ± 0.5, $b = -0.10 \pm 0.003$ ($\pm\sigma$, σ is one standard deviation).

ACPD
13, 22249–22296, 2013

Title Page
Abstract | Introduction
Conclusions | References
Tables | Figures
◀| |▶
◀ ▶
Back | Close
Full Screen / Esc
Printer-friendly Version
Interactive Discussion

ACPD
13, 22249–22296, 2013

Cloud-scale ice supersaturated regions

M. Diao et al.

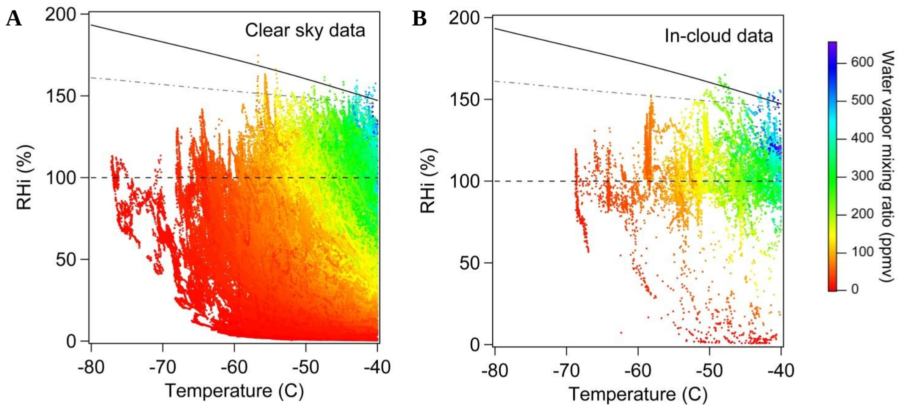

Fig. 5. Distributions of 1 Hz RHi data at various T for clear-sky **(A)** and in-cloud **(B)** conditions. The 1 Hz RHi data are color-coded by H_2O mixing ratio (ppmv). The black solid line and the grey dashed line represent water saturation line and homogeneous freezing line, respectively. Dark dashed line is 100 % RHi.

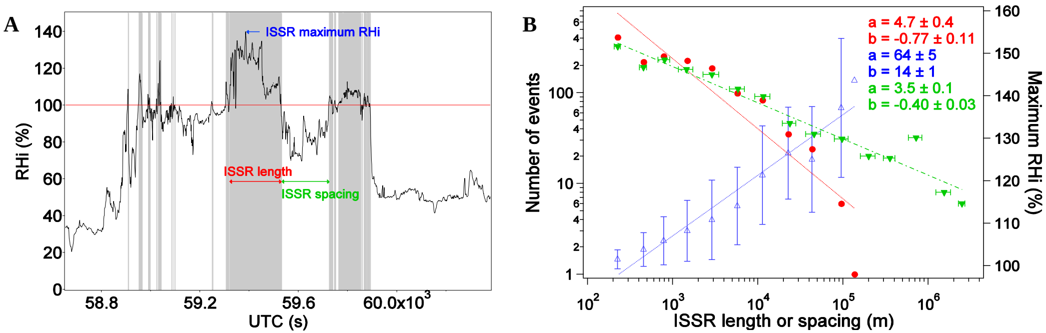

Fig. 6. Aircraft observation of ISSR. **(A)** ISSR 1-D segment lengths (L_ISSR) (grey area) and spacings (L_spacing) (blank area). L_ISSR (or L_spacing) is calculated by multiplying the true air speed with the transect time inside (or outside) the ISSR. The minimum scales are ∼ 230 m (1 second times 230 $m\,s^{-1}$ mean true air speed). Red line denotes RHi = 100 %. **(B)** Both ISSR segment length and spacing are binned by size between 2^i and 2^{i+1} (m), $i = 1, 2, 3...$ The abscissa shows mean L_ISSR and L_spacing values in each bin. The left ordinate shows the number of events (N_e) of ISSR segment length (red dots) and spacing (green triangles) in each size bin. The right ordinate shows the mean RHi_{max} value in each L_ISSR bin (blue triangles). Linear fit of $y = a + b \times x$ is applied to $\log_{10}$(N_e) versus $\log_{10}$(L_ISSR) (red line), $\log_{10}$(N_e) versus $\log_{10}$(L_spacing) (green), and RHi_{max} versus $\log_{10}$(L_ISSR) (blue). For all linear fits in this study $\pm\sigma$ means ± one standard deviation. Intercepts and slopes of the linear fits for all the graphs in this work are represented by values a and b in the legend, respectively.

ACPD
13, 22249–22296, 2013

Cloud-scale ice supersaturated regions

M. Diao et al.

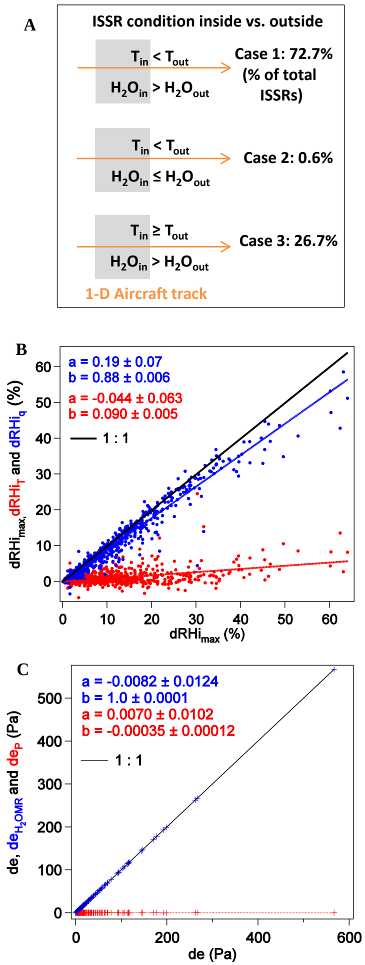

Fig. 7. Correlations between ISSR heterogeneities and T, H_2O horizontal heterogeneities. **(A)** ISSR locations are correlated with three cases of T and H_2O spatial heterogeneities. Grey and blank regions represent ISSRs and the adjacent horizontal (dP<1 hPa) non-ISSRs, respectively. T_{in} and T_{out} represent the mean T value inside and outside (±1 s) ISSRs, respectively; similarly for H_2O_{in} and H_2O_{out}. For 1094 horizontal ISSR segments, 99 % of them correlate with higher H_2O heterogeneities (Cases 1+3) and 73 % correlate with lower T heterogeneities (Cases 1+2). **(B)** $d\mathrm{RHi}_{max}$ is the difference between the RHi_{max} in each ISSR segment and the mean RHi of adjacent (±1 s) non-ISSRs. The slope of $d\mathrm{RHi}_{max}$ (1 : 1 black line) is a linear combination of contributions from horizontal variabilities of T ($d\mathrm{RHi}_T$, red markers, slope: 0.090 ± 0.005) and H_2O ($d\mathrm{RHi}_q$, blue markers, slope: 0.88 ± 0.006). **(C)** Similar to **(B)**, but decompose the changes of H_2O partial pressure term (de, black 1 : 1 line) into the contributions from the changes in total pressure (de_P, red dots) and contributions from the changes of H_2O volume mixing ratio (de_{H_2OMR}, blue dots).

ACPD
13, 22249–22296, 2013

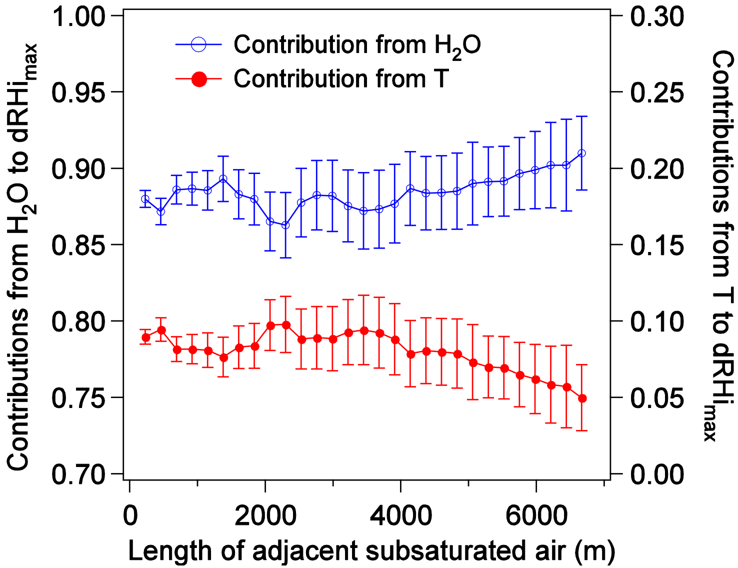

Fig. 8. Contributions from H_2O ($d\mathrm{RHi}_q$, left ordinate) and T ($d\mathrm{RHi}_T$, right ordinate) to $d\mathrm{RHi}_{\mathrm{max}}$ using various scales of horizontally adjacent subsaturated air for comparison. $d\mathrm{RHi}_q$ and $d\mathrm{RHi}_T$ are in red dots and blue circles, respectively. Error bars represent one standard deviation of the linear fit for $d\mathrm{RHi}_q$ or $d\mathrm{RHi}_T$. The large contributions from H_2O to dRHi hold for all length scales of adjacent subsaturated air from ~230 m to 6.7 km.

ACPD
13, 22249–22296, 2013

Title Page
Abstract | Introduction
Conclusions | References
Tables | Figures
◂| |▸
◂ ▸
Back | Close
Full Screen / Esc
Printer-friendly Version
Interactive Discussion

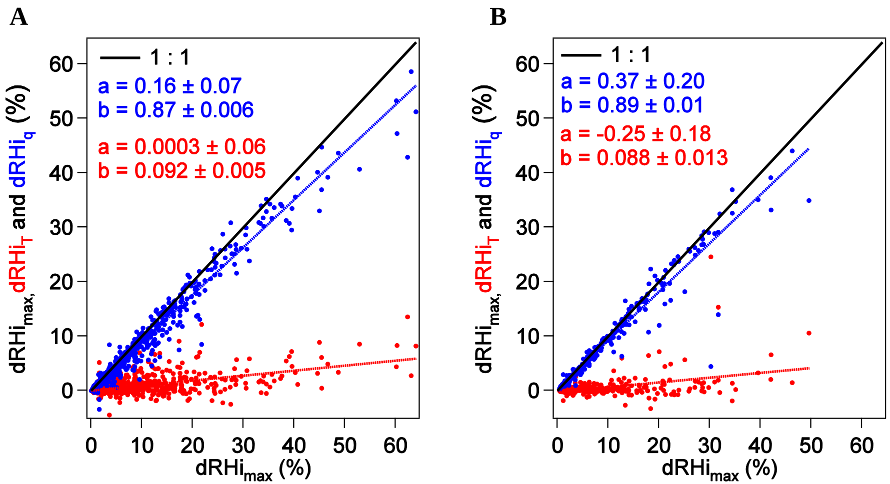

Fig. 9. Contributions from H_2O ($d\mathrm{RHi}_q$) and T ($d\mathrm{RHi}_T$) to the $d\mathrm{RHi}_{max}$ inside the ISSRs in the clear-sky **(A)** and in-cloud **(B)** conditions. The number of ISSRs in clear-sky **(A)** and cloudy **(B)** conditions are 783 and 273, respectively.

ACPD
13, 22249–22296, 2013

Cloud-scale ice supersaturated regions

M. Diao et al.

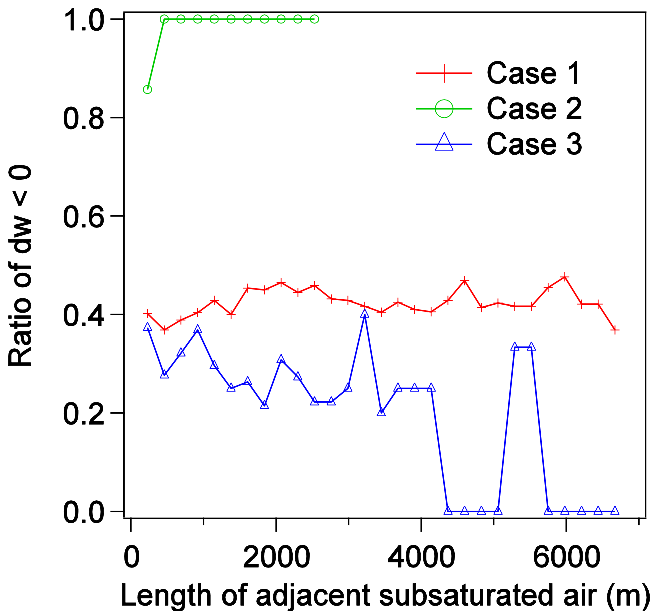

Fig. 10. The ratios of negative relative vertical velocity (*dw* <0) for three cases of ISSRs with respect to various scales of horizontally adjacent subsaturated air. Cases 1, 2, and 3 represent the three types of ISSRs defined in the main text (Fig. 7a), shown in red, green, blue, respectively in the current figure. Cases 1 and 3 both have a significant number of ISSRs with negative *dw* values, regardless of the scale of the adjacent subsaturated air used for comparison. Case 2 has only a small number (≤ 7) of total ISSRs, therefore its *dw* ratio does not significantly influence the overall conclusion. The result shows that most (∼ 60–70 %), but not all, ISSRs move downward relative to the adjacent non-ISSRs.

ACPD
13, 22249–22296, 2013

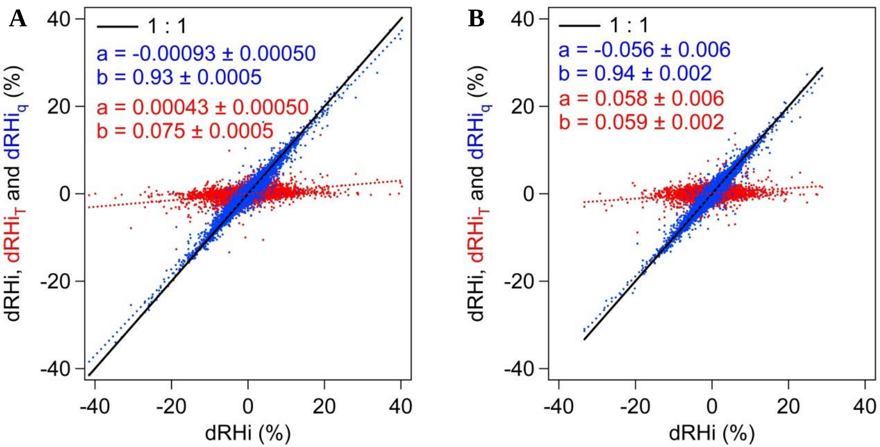

Fig. 11. RHi horizontal variability in non-ISS (subsaturated + saturated) and ISS conditions. **(A)** 1 Hz *d*RHi analyses for non-ISS (sample size $N = 269\,334$); **(B)** 1 Hz *d*RHi analyses for ISS ($N = 17\,834$). The large contributions of H_2O horizontal variability to *d*RHi do not vary significantly between non-ISS and ISS conditions: 0.93 ± 0.0005 (non-ISS) and 0.94 ± 0.002 (ISS).

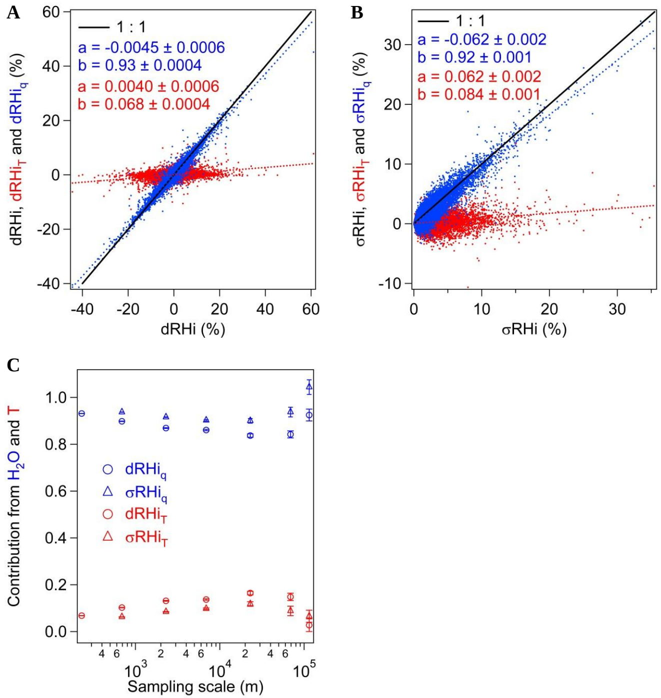

Fig. 12. Contributions to RHi horizontal variability from H_2O and T horizontal variabilities. The horizontal variability (dP<1 hPa) of all RHi is analyzed, including both ISS and non-ISS conditions. Intercept and slope of the linear fits (H_2O: blue dots, T: red dots) are represented by value a and b in the legend, respectively. **(A)** 1 Hz dRHi for all RHi (sample size N = 288 827); **(B)** 1 Hz σRHi at ~2.3 km (10 s) scale for all RHi (N = 57 196); **(C)** scaling of H_2O and T contributions from ~230 m to 115 km (500 s). Sample sizes of dRHi from ~230 m to 115 km are 288 827, 85 875, 20 526, 6189, 1579, 372 and 166, respectively. Sample sizes of σRHi from ~690 m to 115 km are 192 499, 57 196, 18 601, 5186, 1476, 768 and 303, respectively.

ACPD
13, 22249–22296, 2013

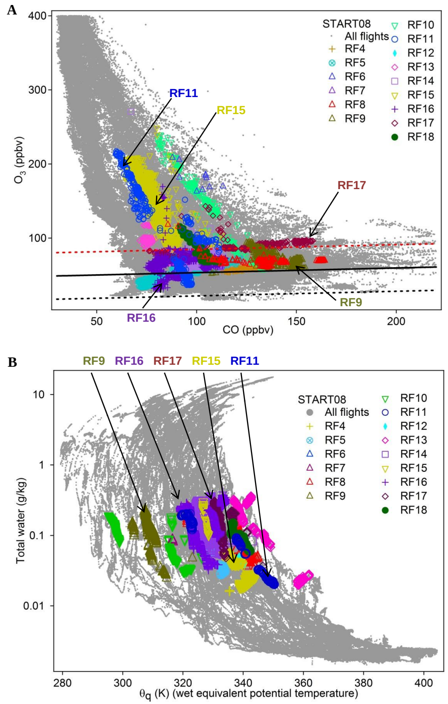

Fig. 13. ISS observations along mixing lines in conservative tracer-tracer correlations. **(A)** O_3-CO correlations from START08 campaign. **(B)** Total water content and θ_q correlations in START08. The horizontal solid black line is the linear fit to the tropospheric branch of all RHi observations and dotted lines are the $\pm 3\sigma$ of the fits. For reference, grey background points in **(A)** and **(B)** show the observations in all T ranges. ISS data are colored by individual flight numbers with the same markers in **(A)** and **(B)**. Because the mixing lines overlap with each other in **(A)** and **(B)**, we highlighted a few straight mixing lines with arrows with colored flight numbers as examples (see arrows with labels in the figure).

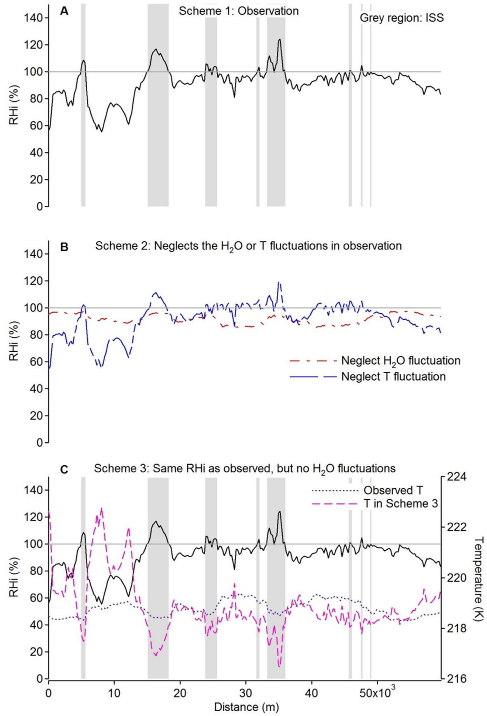

Fig. 14. Example of derivations of ISS spatial variability on a horizontal layer. The horizontal grey solid line denotes RHi = 100 % and grey regions represent ISSRs. **(A)** Scheme 1 is an example of the horizontal distribution of ISS from observation. **(B)** Scheme 2 either neglects H_2O variability or T variability from the observation. The red short dashed line (blue long dashed line) uses the same T (H_2O) variability as observed, but neglects H_2O (T) fluctuations and only considers the mean H_2O (T) value. The result gives no ISS when neglecting H_2O fluctuations. **(C)** Scheme 3 uses T fluctuations to generate the same RHi distribution as observed, but still neglects H_2O fluctuations. The result implies a lower T value in ISSRs (pink dashed line) than the observed T value (purple dotted line).